Electrodeposition of Sr-substituted hydroxyapatite on low modulus beta-type Ti-45Nb and effect on in vitro Sr release and cell response

Romy Schmidt[a], Annett Gebert[a,*], Matthias Schumacher[b], Volker Hoffmann[a], Andrea Voss[a], Stefan Pilz[a], Margitta Uhlemann[a], Anja Lode[b], Michael Gelinsky[b]

[a] *Leibniz Institute for Solid State and Materials Research Dresden (IFW Dresden), Institute for Complex Materials, Helmholtzstr. 20, 01069 Dresden, Germany*
[b] *Technische Universität Dresden (TU Dresden), Faculty of Medicine and University Hospital, Centre for Translational Bone, Joint and Soft Tissue Research, Fetscherstr. 74, 01307 Dresden, Germany*

ABSTRACT

Beta-type Ti-based alloys are promising new materials for bone implants owing to their excellent mechanical biofunctionality and biocompatibility. For treatment of fractures in case of systemic diseases like osteoporosis the generation of implant surfaces which actively support the problematic bone healing is a most important aspect. This work aimed at developing suitable approaches for electrodeposition of Sr-substituted hydroxyapatite (Srx-HAp) coatings onto Ti-45Nb. *Potentiodynamic polarization* measurements in electrolytes with 1.67 mmol/L $Ca(NO_3)_2$, which was substituted by 0, 10, 50 and 100% $Sr(NO_3)_2$, and 1 mmol/L $NH_4H_2PO_4$ at 333 K revealed the basic reaction steps for OH^- and PO_4^{3-} formation needed for the chemical precipitation of Srx-HAp. Studies under *potentiostatic control* confirmed that partial or complete substitution of Ca^{2+}- by Sr^{2+}-ions in solution has a significant effect on the complex reaction process. High Sr^{2+}-ion contents yield intermediate phases and a subsequent growth of more refined Srx-HAp coatings. Upon *galvanostatic pulse-deposition* higher reaction rates are controlled and in all electrolytes very fine needle-like crystalline coatings are obtained. With XRD the incorporation of Sr-species in the hexagonal HAp lattice is evidenced. Coatings formed in electrolytes with 10 and 50% Sr-nitrate were chemically analyzed with EDX mapping and GD-OES depth profiling. Only a fraction of the Sr-ions in solution is incorporated into the Srx-HAp coatings. Therein, the Sr-distribution is laterally homogeneous but non-homogeneous along the cross-section. Increasing Sr-content retards the coating thickness growth. Most promising coatings formed in the electrolyte with 10% Sr-nitrate were employed for Ca, P and Sr *release analysis* in Tris-Buffered Saline (150 mM NaCl, pH 7.6) at 310 K. At a sample surface: solution volume ratio of 1:200, after 24 h the amount of released Sr-ions was about 30–35% of that determined in the deposited Srx-HAp coating. In vitro studies with human bone marrow stromal cells (hBMSC) revealed that the released Sr-ions led to a significantly enhanced cell proliferation and osteogenic differentiation and that the Sr-HAp surface supported cell adhesion indicating its excellent cytocompatibility.

1. Introduction

In the current research on new metallic materials for load-bearing implants for the skeleton system, beta-type Ti-based alloys are considered as being most promising. They exhibit a very good mechanical biofunctionality due to an outstanding combination of low stiffness for the reduction of stress shielding with high strength, fatigue and wear resistance as well as an excellent biocompatibility [1]. These aspects are of particular importance for implants needed for the growing number of patients with systemic bone diseases like osteoporosis which is characterized by reduced bone mass and density as well as micro-

architectural deterioration of bone tissue. This disease demands special measures to support the problematic bone healing process and to ensure high implant reliability [2].

A special focus is on beta-type Ti-Nb alloys with only non-toxic constituents which exhibit with 60–69 GPa much lower Young's modulus values than clinically used implant materials like CP-Ti and Ti-6Al-4V (100 and 110 GPa, respectively) [1,3]. Careful compositional design with beta-stabilizing elements and the development of thermo-mechanical processing strategies for controlled adjustment of micro-structural parameters are effective to further improve the mechanical properties, in particular towards significant materials strengthening

[4–6]. For those alloys very low metal release rates and improved response of human bone marrow stromal cells (hBMSC) in comparison to the established materials were observed [7–9].

Generally, Ti and Ti-based alloys form naturally thin oxide layers which protect the surface against corrosion. Though in many fundamental studies those surfaces are claimed to be bioinert, it is meanwhile established by in vitro and in vivo studies that also Ti (alloy) implants can significantly enhance the inflammatory response and thus, may cause complications in wound healing processes [10,11]. To suppress this and to improve osseointegration the surface of Ti-based implant materials must be suitably modified towards optimum chemistry, roughness, topography etc. [12]. A common approach is the coating with hydroxyapatite (HAp) which is known as bioactive, osteoconductive and biocompatible ceramic [13]. Hydroxyapatite is a calcium phosphate, pure (i.e., stoichiometric) HAp crystallizes in monoclinic, P21/b space group symmetry, with 88 atoms per unit cell and $Ca_{20}(PO_4)_{12}(OH)_4$ stoichiometry. Any precipitation under atmospheric conditions leads to the inclusion of carbonate ions, which necessitate charge compensation and, thus, lead to vacancies, deformations of the lattice and adoption of hexagonal, P63/m space group symmetry, with 44 atoms per unit cell and $Ca_{10}(PO_4)_6(OH)_2$ stoichiometry [14]. The tetrahedral coordinated phosphate anion has a strong covalent bonding character and interacts strongly with neighboring ions. Calcium cations occupy two different lattice sites, Ca(I) is nine-fold coordinated to oxygen ions from phosphate groups and Ca(II) is seven-fold coordinated – with oxygen ions from six phosphate groups and from one hydroxide group [15]. The mineral phase of bone and teeth is assimilated to synthetic hydroxyapatite but differs slightly. Biological apatites can be carbonated and can also contain significant amounts of further foreign ions, either incorporated in the apatite crystal lattice or adsorbed on the crystal surface. The bone structure is thereby flexible in the acceptance of mineral substitutions, e.g. Na, Mg, Zn, Si, Sr. A comparative compilation of trace elements in human bone can be found in [16]. Chemical substitutions in artificial HAp do not only alter its microstructure, stability or crystallinity. For example, Sr-cations Sr^{2+} can be incorporated into the HAp lattice substituting at Ca-sites and thus, forming continuous solid solutions Srx-HAp up to full substitution Sr-HAp [17,18].

Osteoporosis is characterized by an impaired balance of bone resorption by osteoclasts and bone formation by osteoblasts. Strontium is established in systemic osteoporosis therapy – it is known to stimulate bone formation by acting as inhibitor of osteoclastic resorption as well as stimulator of proliferation and differentiation of bone-forming cells [19,20]. A growing number of studies focusses on local delivery of strontium species into a bone defect by integration of strontium in biomaterials like hydroxyapatite, calcium phosphate bone cements or bioglasses [21–23] which in part are also employed as metallic implant coatings.

A commercial method for the coating of implants made of Ti or Ti-6Al-4V is plasma spraying of chemically synthesized HAp [24,25]. However, this clinically accepted process has some limitations as it is difficult to control the layer composition and structure as well as, the processing temperatures are quite high (> 1273 K). Those temperatures are much higher than the beta-transus temperatures and therefore, would lead for example in case of the metastable Ti-45Nb alloy to the precipitation of undesired secondary phases in the beta-microstructure which would increase the Young's modulus. For this new alloy type suitable surface treatment methods at low operation temperatures are needed. Moreover, biomimetic methods for coating deposition based on chemical syntheses of calcium phosphates, hydroxyapatites are widely studied, e.g. as reported in [16,26,27]. Alternative to those methods, cathodic electrodeposition is a time-effective low cost and low temperature method for coating implant surfaces. Moreover, via control of electrochemical parameters it allows even the coating of complex-shaped substrates or of porous structures with inner surfaces [28]. With this technique not only metallic layers can be achieved. By combining

the electrochemical reduction with a subsequent chemical precipitation reaction on the electrode surface in which the reduced species act as reactants, also non-conductive ceramic layers like calcium phosphates, hydroxyapatite, can be deposited. The morphology as well as the phase composition of the obtained layers can be controlled by adjusting the deposition parameters, as it was shown in electrodeposition studies onto stainless steel or Ti-6Al-4V substrates [29,30]. The electrochemical deposition of HAp layers on newly developed beta-type Ti-40Nb was recently demonstrated [28,31]. Especially in the temperature range of 333–353 K and upon potentiostatic polarization conditions adhesive HAp layers with needle- to plate-like morphologies and with thicknesses of several micrometers were deposited. Few first publications report on studies regarding the incorporation of additional metal species into electrodeposited Ca-phosphate layers which either substitute Ca-ions in the crystal structure or form additional phases. Drevet et al. [32] conducted electrodeposition onto Ti-6Al-4V substrates in electrolytes comprising $Ca(NO_3)_2$ and $Sr(NO_3)_2$ in different concentration ratios besides $NH_4H_2PO_4$ (and H_2O_2). The application of long current pulses was found to be effective for depositing calcium-deficient apatite coatings with up to 5% Sr substituting Ca in the structure. But the electrodeposits were of low crystallinity and only additional annealing at 1273 K for 15 h led to mixtures of crystalline Hap and beta-TCP (tricalcium phosphate). Wolf-Brandstetter et al. [33] investigated the co-deposition of Cu-species with Ca-phosphate coatings onto CP-Ti substrates with special focus on the effect of the current pulse parameters. Those control the amounts of generated Ca-phosphate and Cu-species and have an impact on the detailed chemistry and morphology of the nano-needle shaped deposits with consequences for metal release, especially of Cu-ions in synthetic body fluids. However, while more advanced studies e.g. on biomimetic deposition or micro-arc oxidation of Sr-substituted HAp coatings already reported successful in vivo test results, i.e. marked improvements in the behavior of bone tissue formation around Ti implants [34,35], those low temperature electrodeposition techniques are still quite new. They are currently at a stage of gaining a fundamental understanding of reaction mechanisms and the impact of electrochemical parameters on the resulting coating characteristics.

Aim of the present work is to develop suitable approaches for Sr-substitution in electrochemically deposited hydroxyapatite on beta-Ti-45Nb surfaces without additional high temperature treatments. Potentiostatic deposition and galvanostatic pulse-deposition in electrolytes with different Sr-ion concentrations at 333 K are investigated and the reaction processes leading to different coating morphologies and compositions are discussed. Furthermore, first release studies in a physiological solution and first cytocompatibility tests with hBMSC are conducted to analyze selected layer conditions in vitro.

2. Materials and methods

2.1. Electrochemical polarization and deposition studies

Ti-45Nb alloy samples were prepared as substrates for the electrodeposition of Sr-modified Hap. Discs with a thickness of 0.1 cm and a diameter of 1.5 cm were cut from a commercial Ti-45Nb rod (ATI specialty alloys and components, USA). The samples were mechanically ground with SiC paper up to P1200 grit and P4000 grit, respectively, rinsed with distilled water and ethanol and dried in air. For electrochemical studies the samples were mounted in a specimen holder so that the surface area exposed to the electrolyte was 0.95 cm^2.

For the electrolyte, the salts $Ca(NO_3)_2$, $NH_4H_2PO_4$ and $Sr(NO_3)_2$ (Merck Millipore analytical grade) were diluted in de-ionized water. The used salt concentrations are given in Table 1. The substitution of Ca^{2+}-ions by Sr^{2+}-ions in the electrolyte is described by the Sr / (Ca + Sr) ratio calculated from the salt concentrations. The chosen Sr-free electrolyte composition – denominated as Sr0 in this study - is based on studies of Wolf-Brandstetter et al. [33].

Table 1

Salt concentrations and element concentration ratios of the used electrolytes.

Electrolyte	$c(Ca(NO_3)_2)$ [mol/L]	$c(NH_4H_2PO_4)$ [mol/L]	$c(Sr(NO_3)_2)$ [mol/L]	Sr/(Ca + Sr)	(Ca + Sr)/P
Sr0	0.00167	0.001	–	0	1.67
Sr10	0.001503	0.001	0.000167	0.1	1.67
Sr50	0.000835	0.001	0.000835	0.5	1.67
Sr100	–	0.001	0.00167	1	1.67

Accordingly, Sr100 is the Ca-free solution – the Ca-nitrate was completely substituted by Sr-nitrate. The Sr10 and Sr50 electrolytes have a 10% and 50% Sr-salt substitution, respectively. The resulting layers are indicated according to the electrolyte that was used for their deposition. All electrolytes had a pH value of 5.2 at 296 K.

Electrochemical measurements were performed in a double-walled glass cell (Sensortechnik Meinsberg, Germany) which was combined with a thermostat to control a temperature of 333 K. Experiments were carried out with a Solartron SI 1287 electrochemical interface which was connected to the three-electrode cell comprising a working electrode (the sample under study), a platinum net as counter electrode and a Ag/AgCl electrode (SSE, E = 0.197 V vs. NHE) as reference electrode. The electrolyte was constantly stirred with a magnetic stirrer. In order to avoid any precipitation from the electrolytes prior to an electrochemical experiment, only freshly prepared electrolytes were used and fast heating of the stirred electrolyte was done.

Cyclic potentiodynamic polarization studies were conducted using a scan-rate of 1 mV/s. After measuring the open circuit potential (OCP) for 1 h, the sample was polarized negatively from OCP to −2 V vs. Ag/AgCl, then positively back to the OCP. Based on the recorded current density versus potential curves, cathodic potentials were selected for the potentiostatic deposition experiments. For those the OCP was stabilized for 10 min after sample immersion to the electrolyte and then, the electrode potential was stepped to the deposition potential where it was held constant for 3 h. For galvanostatic pulse-deposition, after OCP stabilization a cathodic current density was applied according to the following scheme (after [32]): $j_d = -15$ mA/cm^2 was applied for $t_{on} = 20$ s followed by a break ($j_b = 0$ mA/cm^2) for $t_{off} = 30$ s. This cycle was repeated 96 times. After the deposition experiments, the coated substrates were rinsed with distilled water and dried at room temperature in air. Each electrochemical measurement was repeated at least three times to ensure a high level of reproducibility.

2.2. Characterization of the electrodeposited layers

Grazing incidence X-ray diffraction (XRD) analysis was carried out by means of a Philips X'Pert Pro thin film diffractometer in order to investigate the phase composition of the deposited layers. Cu-Kα radiation was used (40 mA, 40 kV) with an incidence angle of 2° and the 2θ range was from 15 to 60°. Phase analysis was done with the ICSD database.

High resolution scanning electron microscopy (SEM) analyses were carried out using a Zeiss Leo Gemini 1530 SEM equipped with an energy dispersive X-ray (EDX) detector (X-Flash SSD, Bruker). To receive the SE-contrast (SE – secondary electron) images with high quality, the ceramic-type deposits were covered with a very thin Au layer by means of sputtering. EDX mappings were conducted to analyze the lateral distribution of Ca, P, O and Sr in the coatings.

Element depth distribution profiles of the deposited layers were obtained by means of glow discharge optical emission spectroscopy (GD-OES) depth profiling technique. A radio-frequency (rf) source designed and built in-house was employed to produce sputtering craters of 1 mm in diameter. The construction is based on the Universal Sample Unit from Spectruma Analytik GmbH (Hof, Germany). Discharge parameters of 500 V anode voltage (resulting in about 425 V amplitude

and 425 DC bias) and 2 hPa Ar pressure result in a sufficiently flat crater shape and an erosion rate of about 100 nm/s. Intensity-time curves of selected emission lines (H 121.567 nm, O 130.217 nm, N 149.262 nm, P 178.280 nm, Nb 319.340 nm, Ti 337.279 nm, Ca 393.367 nm, Sr 421,552 nm) were recorded using a high sensitive Photomultiplier (PMT) based GDA750 (Spectruma Analytik GmbH).

2.3. Wet chemical analysis for deposit characterization and release studies

Inductively coupled plasma optical emission spectrometry (ICP-OES) using an ICP-OES iCAP 6500 Duo View (Thermo Fisher Scientific) was employed for the determination of element concentrations in electrodeposited layers and in a physiological solution. In case of the chemical analysis of galvanostatically deposited layers, for one layer type four control samples were used. Each sample was dissolved in a beaker with concentrated HNO$_3$ (65%, analytical grade, Merck Millipore) and subsequently, distilled water was added to obtain in total a solution of 50 g mass. Each solution was analyzed four times for the determination of Ca, P and Sr concentrations. Release studies of Ca, Sr and P from electrodeposited layers into a physiological solution were conducted based on DIN EN ISO 10993-15 [36] "Biological evaluation of medical devices – Part 15: Identification and quantification of degradation products from metals and alloys". As a complex simulated body fluid does not allow a reliable metal ion trace concentration analysis in solution, samples were immersed in TBS (Tris-Buffered Saline, BioUltra, tablets for 500 mL, Fa. Sigma-Aldrich) which is based on 150 mM NaCl (~0.9% NaCl) with pH 7.6 at a temperature of 310 ± 1 K. For the simulation of static solution conditions, the ratio of sample area (cm^2)/immersion solution (ml) was 1:1 and after 1 h, 4 h, 24 h and 7 days immersion the solution was analyzed. For exemplarily simulating dynamic solution conditions, a ratio of sample area (cm^2)/immersion solution (ml) was 1:200 was chosen and after 24 h immersion the solution was analyzed. For each test condition four control samples were immersed in TBS and two blind solutions were analyzed, each solution was analyzed three times. At the given test conditions the quantification limits for the elements released in TBS are 0.00020 μmol/cm^2 for Ca, 0.00019 μmol/cm^2 for Sr and 0.00098 μmol/cm^2 for P.

2.4. In vitro studies with human bone marrow stromal cells (hBMSC)

The effect of layers from galvanostatic pulse experiments on cellular processes was determined in an in vitro study with hBMSC, isolated from the bone marrow of one healthy male donor after obtaining informed consent (kindly provided by the Medical Clinic I, Dresden University Hospital). The ethics commission of Technische Universität Dresden approved the application of the hBMSC for in vitro experiments. Cells were cultured in alpha-MEM containing 9% FCS, 10 U/ml penicillin, 100 μg/ml streptomycin and 1% L-glutamine; osteogenic differentiation was induced by addition of 0.1 μmol dexamethasone, 50 μM beta-glycerophosphate and 5 mM ascorbic acid 2- phosphate (osteogenic supplements (OS); Sigma-Aldrich).

2.4.1. Indirect cell culture

The effects of the ions released from the electrodeposited layers were evaluated in an indirect cell culture setup. Coated and uncoated reference samples were immersed in 1 ml/sample cell culture medium with osteogenic supplements (OS+) for 24 h. Simultaneously, hBMSC were seeded in 48 well-plates (8 × 10^3/well) and allowed to adhere for 24 h. From day 1 on, medium from the immersed samples was transferred onto the cell layers (300 μl/well; $n = 3$) every 3 to 4 days, fresh medium was added to the samples. As control, medium which was not in contact with any material was used. After 1, 14 and 21 days, cell layers were frozen until analysis.

2.4.2. of hBMSC proliferation and osteogenic differentiation

Proliferation was determined by means of intracellular lactate dehydrogenase (LDH) activity as described [37]. In brief, after cell lysis in 1% Triton X-100/PBS (50 min on ice including 10 min ultrasonication), LDH activity was measured from aliquots of the lysates using the CytoTox 96 Non-Radioactive Cytotoxicity Assay (Promega) and correlated with the cell number using a calibration line. Osteogenic differentiation was characterized by alkaline phosphatase (ALP) activity measurement in aliquots of the lysates as described [37]. In brief, p-nitrophenyl phosphate (pNpp, Sigma-Aldrich) was converted to p-nitrophenolate (pNp) which was photospectrometrically quantified; the amount of pNp was related to the cell number in each lysate (calculated from LDH activity) to gain the specific ALP activity in μmol pNp/30 min/10^6 cells.

2.4.3. Direct contact culture

For evaluation of the cell morphology in contact with electrochemically coated vs. uncoated Ti-45Nb surfaces, samples were immersed in cell culture medium for 2 h and seeded with $4 \cdot 10^4$ cells/sample. During cultivation for 14 days, cell culture medium (OS+) was changed every 3 to 4 days. After 1, 7 and 14 days, samples were washed with PBS and fixed in 3.7% formaldehyde/PBS for fluorescence microscopy. Cell nuclei and actin cytoskeleton were stained with DAPI (4′,6-diamin-2-phenylindol, Invitrogen) and Alexa Fluor 488® phalloidin (Invitrogen); fluorescence microscopy was performed with a Keyence BZ9000E (Keyence, Japan).

3. Results and discussion

3.1. Potentiodynamic polarization analyses

Potentiodynamic polarization measurements were conducted in the cathodic regime to analyze the reaction steps at the Ti-45Nb substrates in the $Ca(NO_3)_2$ and $NH_4H_2PO_4$ electrolytes without (Sr0) and with Sr$(NO_3)_2$ substitutions (Sr10, Sr50, Sr100) which are specified in Table 1. In Fig. 1 examples of current density vs. potential curves which were obtained in the Sr-free (Sr0) and in the Sr10 electrolyte are shown. In this negative potential regime, an increasing rate of the reduction reaction of water (eq. (1.4)) with negative potential shift leads to a general curve shape which is dominated by a gradual increase of the cathodic current density. Nevertheless, in accordance with literature data one may formally distinguish characteristic potential regions which are ascribed to the following reactions [38–40]:
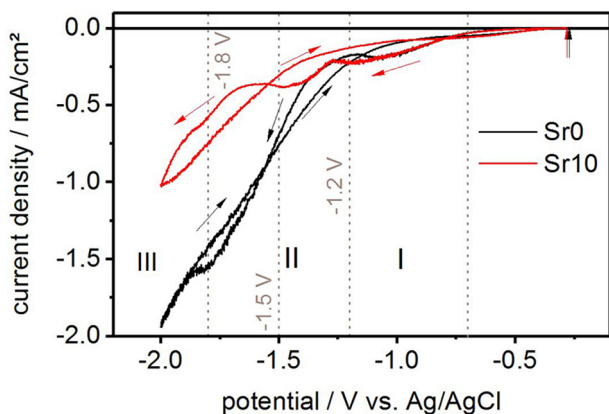
Region I

$$NO_3^- + H_2O + 2e^- \rightarrow NO_2^- + 2OH^- \tag{1.0}$$

Fig. 1. Cathodic current density vs. potential curves recorded on Ti-45Nb electrodes in water-based electrolyte Sr0 with 1.67 mM $Ca(NO_3)_2$ and 1 mM $NH_4H_2PO_4$ and in electrolyte Sr10 with 10% substitution of $Ca(NO_3)_2$ with Sr$(NO_3)_2$ (see Table 1) at 333 K and at a scan-rate of 1 mV/s; the vertical arrows mark the OCP.

$$(O_2 + 2H_2O + 4e^- \rightarrow 4OH^-) \tag{1.1}$$

Region II

$$2H_2PO_4^- + 2e^- \rightarrow 2HPO_4^{2-} + H_2 \tag{1.2}$$

$$2HPO_4^{2-} + OH^- \rightarrow PO_4^{3-} + H_2O \tag{1.3}$$

Region III

$$2H_2O + 2e^- \rightarrow H_2 + 2OH^- \tag{1.4}$$

Due to low concentrations of reactants in solution, mass transport-controlled reduction reactions (1.0)–(1.3) with limited rate are to be expected which will be superimposed with the main reaction (1.4). Also, in this mixed process the kinetics of the electrochemical reaction steps will be influenced by the beginning chemical precipitation of non-conductive coatings (1.5) which gradually block the electrode surface. Therefore, expected characteristic peaks or shoulders in the polarization curves corresponding to (1.0)–(1.3) may be in each electrolyte only more or less pronounced and may occur variably in wider potential ranges. Thus, in practice formal regions I and II are often not clearly identifiable.

In the *Sr0 electrolyte*, in *region I* (−0.7 to −1.2 V vs. Ag/AgCl) the nitrate (NO_3^-) reduction according to Eq. (1.0) is the main source for the generation of hydroxide ions (OH^-). Besides, a minor contribution from the reduction of small concentrations of dissolved oxygen to hydroxide ions according to Eq. (1.1) is taken into account. In *region II* (−1.2 to −1.8 V vs. Ag/AgCl) the hydrogen reduction and protolytic reaction of the dihydrogen phosphate ion ($H_2PO_4^-$) leads to the formation of the hydrogen phosphate ion (HPO_4^{2-}) (Eq. (1.2)). The presence of hydroxide ions generated in Eqs. (1.0) and (1.1). enables a further protolytic reaction to form the phosphate ion (PO_4^{3-}) according to Eq. (1.3). *Region III* (from −1.8 V vs. Ag/AgCl) is dominated by the reduction of water according to Eq. (1.4). In consequence of these reduction steps, the pH value in the vicinity of the Ti-45Nb cathode increases corresponding to OH^--ions which are adsorbed at the cathode surface. Ca^{2+}-ions migrate to the cathode surface and cause a precipitation reaction with formed PO_4^{3-}- and OH^--ions to a Ca-phosphate, hydroxyapatite, according to reaction (1.5):

$$10Ca^{2+} + 6PO_4^{3-} + 2OH^- \rightarrow Ca_{10}(PO_4)_6(OH)_2 \tag{1.5}$$

In the reverse potential scan no significant reaction peaks are visible indicating that the formed products are electrochemically stable. Previous works showed for similar electrolytes that HAp formation favorably takes place in a potential region from −0.4 to −1.6 V vs. Ag/AgCl [38,41]. In the present study in Sr0, a potential of −1.2 V vs. Ag/AgCl was chosen for further deposition experiments. This is within potential regions I and II and far more positive than *region III* which is dominated by the cathodic water decomposition with strong pH value change.

When substituting 10% of Ca-nitrate concentration in the electrolyte with *Sr-nitrate (Sr10)*, the current density vs. potential curve reveals a similar cathodic response. The overall current density level is decreased indicating that the overall cathodic reduction rate is reduced. Furthermore, in the potential *regions I and II* two reaction peaks (at about −1.2 V and −1.5 V vs. Ag/AgCl) are detectable which are attributed to reactions 1.0(1.1) and (1.2)(1.3), respectively. The second reaction peak at −1.5 V vs. Ag/AgCl is more pronounced in the Sr10 electrolyte than in Sr0. This suggests an impact of Sr^{2+}-ions on the rate of the hydrogen reduction and related protolytic reactions with an expected effect on the precipitate characteristics. Ca and Sr are chemically quite similar and thus, it can be assumed that Sr^{2+}-ions likewise take part in the HAp precipitation process described above (eq. (1.5)) and as suggested in [32] leading to a Srx-HAp compound. From this polarization behavior in the Sr10 electrolyte shown in Fig. 1, a deposition potential of −1.5 V vs Ag/AgCl was selected for further studies.

The Sr-nitrate content in the electrolyte was further increased up to 100% (i.e. Ca-nitrate completely substituted by Sr-nitrate). Fig. 2
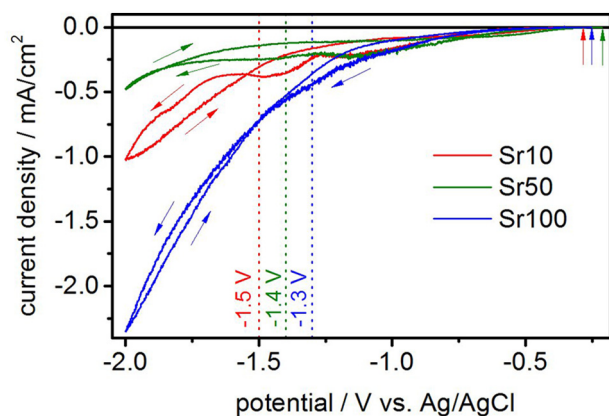
Fig. 2. Cathodic current density vs. potential curves recorded on Ti-45Nb electrodes in water-based electrolyte Sr10, Sr50 and Sr100 with 10%, 50% and 100% substitution of $Ca(NO_3)_2$ with $Sr(NO_3)_2$ (see Table 1) at 333 K and at a scan-rate of 1 mV/s; the vertical arrows mark the OCP.

Fig. 3. Current density transients of potentiostatic polarizations conducted at the indicated potentials in electrolytes Sr0, Sr10, Sr50 and Sr100 at 333 K; inset: initial transient period in Sr100 electrolyte.

comparatively shows current density vs. potential curves recorded in electrolytes with 10, 50 and 100% Sr-nitrate. The increasing Sr^{2+}-ion content in the solution changes the reaction process. When using the Sr50 electrolyte, the overall current density level decreases further compared to that measured in the Sr0 and Sr10 electrolytes. Moreover, the reaction steps in potential *regions I and II* are not that pronounced anymore. The simultaneous presence of Sr^{2+}-ions and Ca^{2+}-ions in the electrolyte has obviously an inhibiting effect on the overall charge transfer on the surface of the Ti-45Nb cathode and also, on the stepwise dihydrogen phosphate ion transformation into phosphate ion (Eqs. (1.2) and (1.3)). Nevertheless, from the current density vs. potential curves recorded in electrolyte Sr50 a deposition potential of -1.4 V vs. Ag/AgCl was derived which was formally defined in potential *region II*. When completely substituting the Ca-nitrate by Sr-nitrate (electrolyte Sr100) the overall current density level is quite high again and is similar to that attained in Sr-free electrolyte (Sr0). The discrete reaction steps are barely visible. A deposition potential of -1.3 V vs. Ag/AgCl was defined. In Sr100, the formation of Sr-HAp is expected corresponding to the formation of Ca-based HAp in the Sr0 electrolyte. In both cases cathodic reactions on the Ti-45Nb surfaces are less inhibited compared to the simultaneous presence of Sr^+- and Ca^{2+}-species in the electrolyte.

Altogether, due to the differences in the potentiodynamic polarization curves recorded in the various electrolytes (Figs.1, 2), for potentiostatic deposition tests in Sr0, Sr10, Sr50 and Sr100 potentials were chosen which are within potential regions I and II (and away from region III) and which correspond to a similar cathodic current density level in a range of 0.2–0.4 mA/cm^2.

3.2. Potentiostatic deposition and layer characterization

Potentiostatic deposition experiments were carried out by stepping the electrode potential from OCP to a cathodic potential which was identified from the previous polarization studies (Section 3.1). Exemplary current density transients recorded in the different electrolytes are shown in Fig. 3. Considering the reaction mechanism for the HAp formation in Section 3.1, those reflect in principle only the electron transfer reaction steps. But chemical reaction steps leading to non-conductive precipitates on the Ti-45Nb substrate can have an impact on their kinetics.

In the *Sr0 electrolyte*, the current density transient reveals after the initial double layer recharge a maximum of ~0.6 mA/cm^2 at ~500 s followed by a gradual current density decay. Besides the nitrate (and oxygen) reduction (equation 1.0 (1.1.)), this maximum may be mainly ascribed to the superimposed steps of the phosphate ion formation (Eqs.
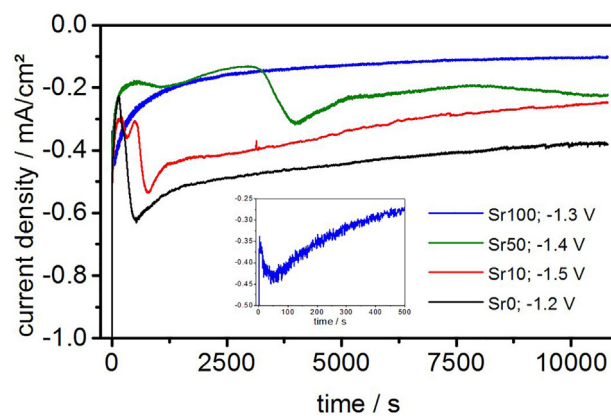
(1.2), (1.3)). In consequence, a chemical precipitation (Eq. (1.5)) is possible which leads to a gradual Ti-45Nb surface blocking with a non-conductive Ca-phosphate. In the *Sr100 electrolyte*, the transient reflects a similar principle behavior, but the maximum occurs much earlier, i.e. already after 45 s, and is with ~0.43 mA/cm^2 significantly smaller. The subsequent current density decay to smaller values is faster. This suggests a faster precipitation of a non-conductive Sr-phosphate layer with more pronounced blocking effect. However, studies based on chemically synthesized apatites (equilibrium conditions) revealed that the solubility of crystalline Sr-HAp in salt solutions is higher than that of Ca-HAp which would contradict the above conclusion [18]. The formation of Ca- or Sr-phosphate phases proceeds via a variety of intermediate phases, e.g. complexes or amorphous phases which nucleate preferentially [18] and those can transform gradually into crystalline Ca- or Sr-apatite phases by hydrolysis [42,43]. Electrochemical reactions proceed at non-equilibrium. With the current density transients mainly the early stages of the deposition process are followed at which intermediate phosphate phases with low crystallinity may form at the Ti-45Nb substrates which do not exhibit the properties of the equilibrium phases.

In the mixed *electrolytes Sr10 and Sr50*, the current density transients comprise 2 (or 3) maxima which may be attributed to the timely resolved reactions (Eqs. (1.0)–(1.3), Section 3.1). Especially in Sr50 these peaks are shifted to longer times and the overall current density level is much lower than that measured in Sr0 and Sr10. In the mixed solutions a retarded cathodic reaction rate is observed with increasing Sr^{2+}-ion fraction in potentiodynamic and in potentiostatic polarization mode. Formally, the formation of Sr-substituted Ca-phosphate ($-$hydroxyapatite) (Srx-HAp) is expected. As the ionic radius of Sr is larger than that of Ca (Sr^{2+} = 0.116 nm, Ca^{2+} = 0.100 nm [44]), this could lead to a steric hindrance of the growing HAp lattice during the precipitation reaction. Moreover, for chemically synthesized crystalline Srx-HAp phases an increasing solubility with increasing Sr-content was detected [18]. Again this contradicts the observed behavior under electrochemical conditions. Thus, also here, we may assume the early formation of intermediate phases with low crystallinity which have a stronger impact on the electron transfer reactions than those forming in Sr-free electrolyte.

In all cases, potentiostatic deposition leads to an early formation of layers which can block the Ti-45Nb surfaces and retard further reduction reactions. Consequently, limited layer growth must be expected. Figs. 4 and 5 show top-view SEM images and XRD patterns of coatings which were deposited in the four electrolytes under potentiostatic control for 3 h. Typical SEM and XRD results of as-ground Ti-45Nb substrate surface states are shown in [7–9,31]. In the Sr10 electrolyte (Fig. 4b), similar as in the Sr0 electrolyte (Fig. 4a, see also [31]) brittle
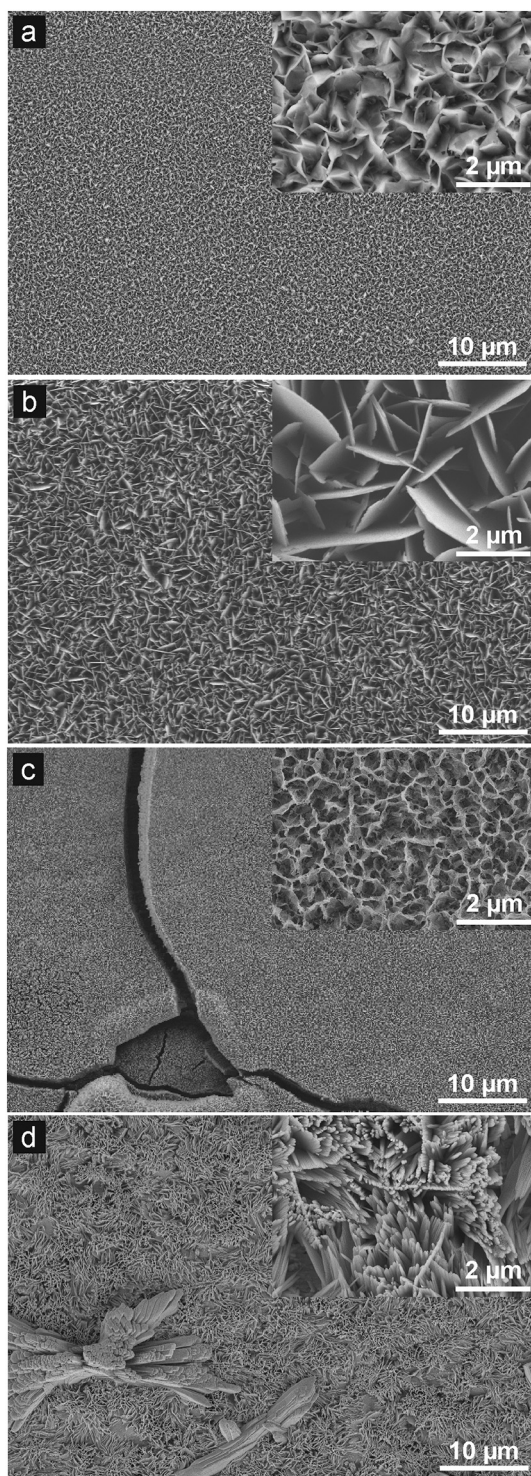
Fig. 5. TF-XRD patterns (incidence angle 2°) of layers potentiostatically deposited at the indicated potentials (all vs. Ag/AgCl) in electrolyte Sr0, Sr10, Sr50 and Sr100 (see Table 1) at 333 K on Ti-45Nb; the indicated lattice planes belong to the HAp phase (PDF: 01–071-5048) unless indexed with beta-Ti-45Nb and "?" indicate not identified reflections.

Fig. 4. SEM images (SE contrast) of potentiostatically deposited layers on Ti-45Nb in electrolyte Sr0 at −1.2 V (a), in electrolyte Sr10 at −1.5 V (b), in electrolyte Sr50 at −1.4 V (c) and in electrolyte Sr100 at −1.3 V (d) (all potentials vs. Ag/AgCl).

coatings with mainly plate-like morphology are observed. XRD analysis revealed that the layers consist of hydroxyapatite as the main phase. The most pronounced reflection at around 26° indicates a {002}-orientation of the deposited HAp crystals on the metallic substrate. This is similar to what was reported before for the electrodeposition of HAp on Ti, Ti-Nb and Ti-6Al-4V [31,45–47]. However, at least two or more small reflections occur which must be attributed to non-identifiable
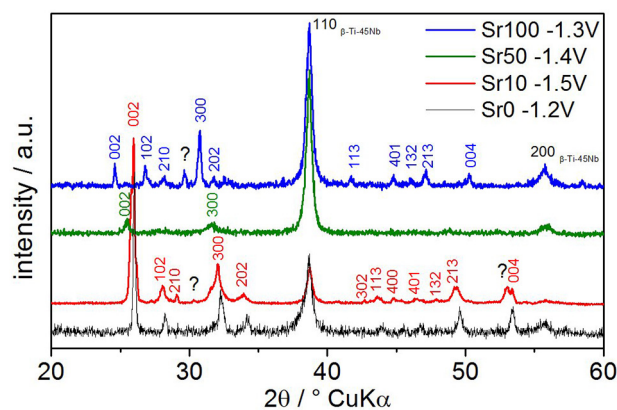
secondary phases. This supports the idea which was earlier developed after FIB cutting of a HAp coating cross section [31] that, upon potentiostatic deposition initially intermediate phases of low crystallinity form on the beta-type alloy substrates. At a later stage those can act as seed-layer for the chemical precipitation of (Sr-substituted) hydroxyapatite with crystalline morphology. Those layers have typically a micrometer thickness, e.g. ~3–5 μm for HAp layers formed at −1.2 V for 3 h. Their adhesion to a mechanically ground Ti-Nb surface was evaluated by scratch testing revealing a critical loading of about 9 N. Coating failure was observed mainly upon severe plastic deformation of the substrate [31].

When increasing the Sr-content in the electrolyte to 50%, the resulting layer yields weak diffraction peaks which indicate only limited crystallinity (Fig. 5). Accordingly, with SEM (Fig. 4c) denser and more brittle coatings with much more refined spongy-like Hap morphology are detected. For layers forming in the electrolyte Sr100, the transition to a very fine needle-like morphology (Fig. 4d) is observed. These layers are relatively dense. XRD patterns in Fig. 5 reveal a clear shift of the diffraction peaks for the apatite phase to smaller diffraction angles with increasing Sr-content in the electrolyte. This indicates the incorporation or complete substitution of Sr-species in the hydroxyapatite phase whereby larger Sr-ions on Ca-sites cause an expansion of the hexagonal lattice and thus, an increase of the lattice parameter.

Altogether, this confirms that partial or complete substitution of Ca^{2+}-ions by Sr^{2+}-ions in the electrolyte greatly effects the complex electrochemical-chemical formation of hydroxyapatite under potentiostatic control with consequences for the layer properties. High Sr-contents seemingly yield an early precipitation of intermediate layers and a subsequent growth of more refined apatite coatings. Chemically synthesized hydroxyapatite can grow in very different morphologies – this depends very sensitively on the particular growth conditions [14,26]. Upon potentiostatic deposition, pH value and phosphate ion concentration in the vicinity of the Ti-45Nb substrate vary with time. Together with the different impact of the cations on the formation of intermediate and final apatite phases this yields a complex pattern of influencing factors. Therefore, it is difficult to clarify the coating process in these electrolytes in detail.

3.3. Galvanostatic pulse-deposition and layer characterization

In further studies cathodic current density pulses were applied for coating formation on the Ti-45Nb substrates. Under galvanostatic conditions constantly higher reaction rates for PO_4^{3-}-ion and OH^--ion formation (Eqs. (1.0)–(1.4)) are enforced which have an impact on the
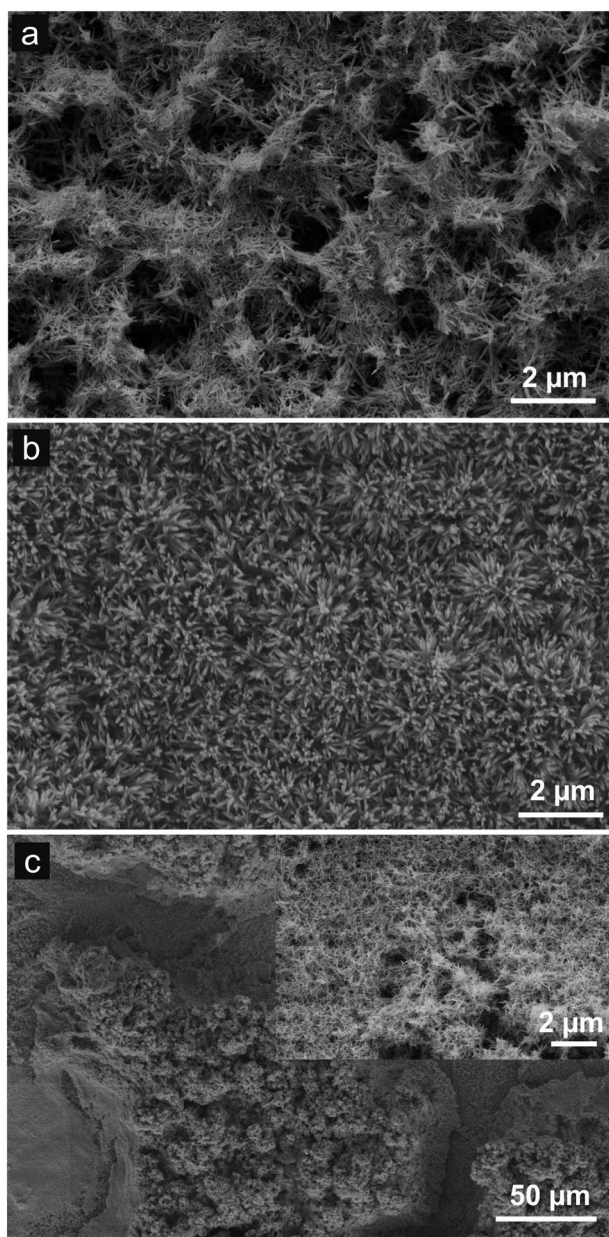
Fig. 7. TF-XRD pattern (incidence angle 2°) of layers galvanostatically pulse-deposited with $j_d = -15\,mA/cm^2$ on Ti-45Nb in the electrolytes Sr10, Sr50, Sr100 (see Table 1); the indicated lattice planes belong to the HAp phase (PDF: 01–071-5048) unless indexed with beta-Ti-45Nb.

Typical SEM images and XRD patterns of coatings obtained in the different electrolytes are shown in Figs. 6 and 7, respectively. There is no significant impact of the Sr- content in the electrolyte on the precipitate morphology, all deposits exhibit a fine needle-like morphology with structure sizes of around 200–300 nm. The repeatedly interrupted process of nucleation and growth of precipitates at assumed nearly constant concentrations of reactants leads to structure sizes which are generally much smaller than those of the potentiostatically deposited layers (Fig. 4). Since at these negative potentials the deposit formation is superimposed by severe water decomposition, the layers in particular in Sr10 electrolyte have micrometer-sized holes which originate from detaching hydrogen bubbles. The Sr50 layers are thinner than those deposited in the Sr10 electrolyte but they also show a fine needle-like morphology (Fig. 6b). The Sr100 layers are inhomogeneous in thickness and morphology (Fig. 6c). Compared to the coatings formed potentiostatically, the crystallinity of all layers is quite high. The XRD reflections correspond only to the hydroxyapatite phase and are clearly pronounced (Fig. 7). Also here, the reflections of the HAp phase are shifted to smaller angles with increasing Sr-content in the electrolyte indicating the incorporation of large Sr-ions in the hexagonal lattice.

In addition, energy dispersive X-ray spectroscopy (EDX) analysis of the coatings was conducted to evaluate especially the presence of Sr-species. The element mappings of Sr10 and Sr50 deposits revealed a laterally homogenous distribution of Sr-species in the layer; exemplarily results for a Sr50 layer are shown in Fig. 8. Because of their morphological inhomogeneity, the EDX analysis of Sr100 layers yielded an inhomogeneous Sr distribution. For the Sr10 layers a Sr/(Ca + Sr) concentration ratio of 0.05 and for the Sr50 layers a Sr/(Ca + Sr) ratio of 0.26 was determined. When comparing this with the concentration ratios in the electrolytes Sr10 and Sr50 with a Sr/(Ca + Sr) ratio of 0.1 and 0.5 (Table 1), respectively, this analysis states that only about half of the Sr-species provided in the electrolyte were incorporated into the layers. Furthermore, the Sr-content in the deposit increases with increasing Sr-content in the electrolyte. Hydroxyapatite has a theoretical Ca/P ratio of 1.67. The (Ca + Sr)/P ratios of the obtained Sr10 and Sr50 layers were determined to be 1.69 and 1.53, respectively.

Furthermore, the element distributions (Ca, Sr, P, O and H) along the cross sections of the deposits Sr10 and Sr50 were investigated by means of the GD-OES depth profiling. Plots of the intensities of the element-specific spectral emission lines vs. the sputter time are in Fig. 9. In Fig. 9a, the depth profile of a Sr10 layer is shown. Stable sputtering of the Hap layer started after ~8 s and is associated with an increase of the Ca, P, O and H signals while the Sr signal rises only weakly. Sputtering was stopped when a major drop in the Ca and P signals and an increase in the Ti and Nb signals were detectable. The

Fig. 6. SEM images (SE contrast) of layers galvanostatically pulse-deposited with $j_d = -15\,mA/cm^2$ on Ti-45Nb in electrolytes Sr10 (a), Sr50 (b) and Sr100 (c) (see Table 1).

subsequent chemical precipitation reaction (Eq. (1.5)) and thus, on layer morphology and growth rates. According to earlier studies [32,33], a galvanostatic pulse-deposition mode was used. Current density pulses of $-15\,mA/cm^2$ were applied for 20 s with intermissions of 30 s under open circuit conditions. During the latter, reactive species in the electrolyte are transported towards the cathode surface and thus, local depletion of reactants is avoided. Those experiments were conducted in the Sr-nitrate substituted electrolytes with up 96 current density pulses. The potential responses (not shown here) are quite uniform, i.e. during pulse-on time rapidly nearly constant potential values establish. In the Sr10 electrolyte this value is initially ~ −5.3 V vs. Ag/AgCl and shifts to ~ −6.8 V vs. Ag/AgCl at the last pulses. In the Sr50 and Sr100 electrolytes constantly a potential level of ~ −6.5 V and −5.6 V vs Ag/AgCl is attained at each pulse. At these negative potentials, the water decomposition (Eq. (1.4)) is predominant. During pulse-off periods in all cases the potential switches back to near to OCP condition.
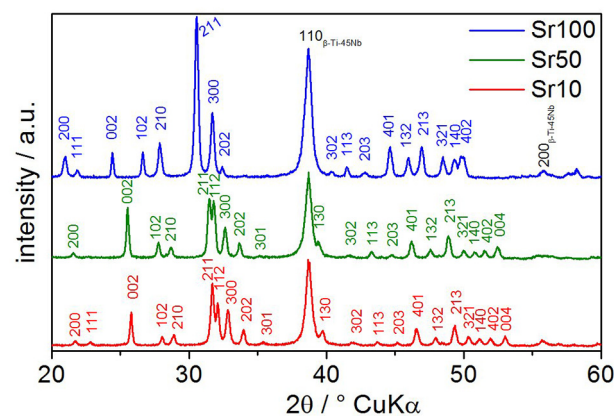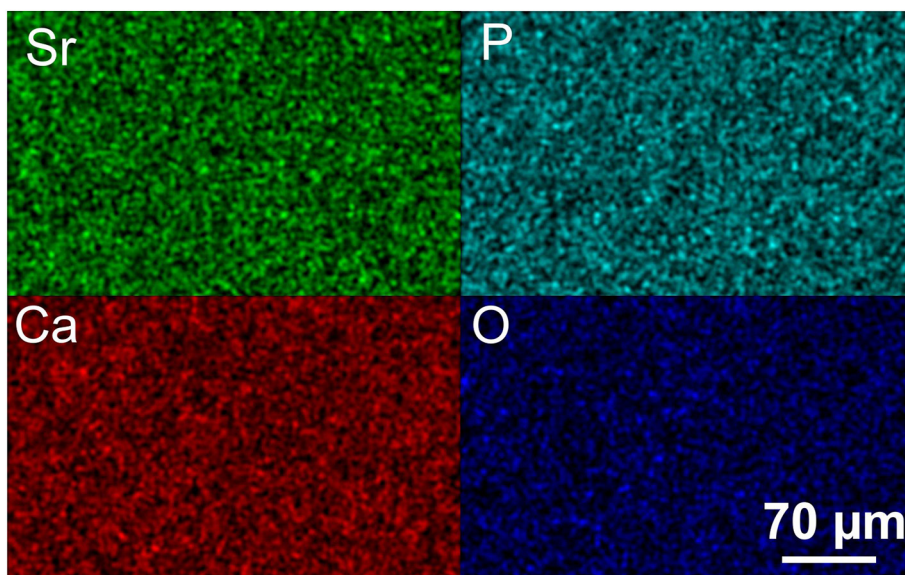
Fig. 8. EDX mapping of a layer, galvanostatically pulse-deposited onto Ti-45Nb in Sr50 electrolyte.
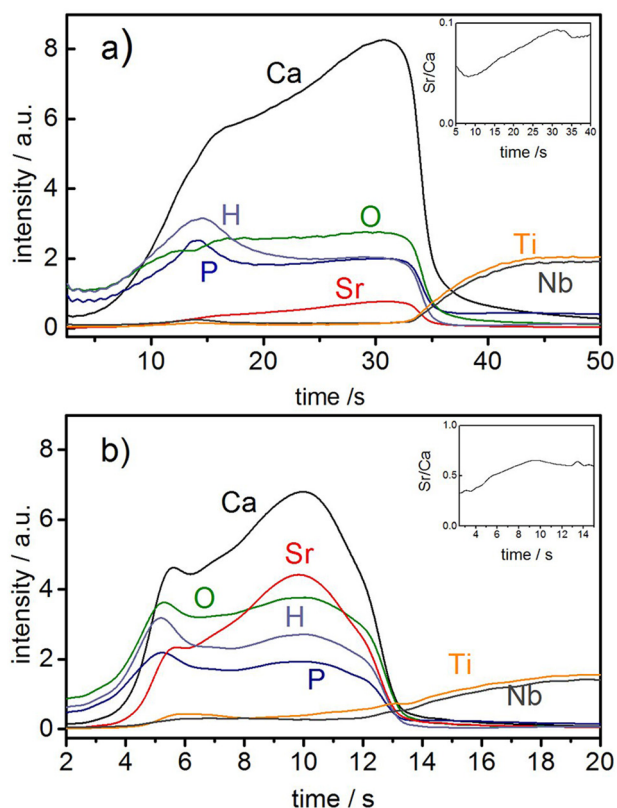

Fig. 9. GD-OES element distribution depth profile analysis of layers galvanostatically pulse-deposited onto Ti-45Nb in electrolyte Sr10 (a) and electrolyte Sr50 (b); insets: Sr/Ca ratio along the cross-section of the layer.

relative intensities of Ca, Sr and P do not change simultaneously with sputter time which is a hint that a stoichiometric Hap phase may not be present throughout the whole coating thickness. Furthermore, the deposited layer is on top dominated by pores and holes (Fig. 6a), but a denser layer could be underneath the visible region which leads to an increase of the Ca, Sr and P signals near to the substrate. The Sr/Ca ratio in the inset of Fig. 9a reveals an inhomogeneous distribution in the layer thickness with an increase of the Sr fraction at the inner layer regions. From previous studies [31] a sputter rate of 100 nm/s was used

and for the Sr10 layer a thickness of around 3 μm was estimated.

In Fig. 9b the depth profile of a Sr50 layer is shown. Here, stable sputtering of the Hap layer started after ~5 s. Compared to the Sr10 layer, the general Sr/Ca ratio in the Sr50 layer is considerably higher (inset in Fig. 9b) implying that the Sr content in the Sr50 layer is higher. This confirms the trend which was concluded from EDX analysis. Furthermore, the intensities of Ca and Sr decrease during sputtering before they rise again which indicates a two-layered structure of the deposit. The Sr50 layer is much thinner than the Sr10 layer which can be derived from the shorter sputter time, a layer thickness of only ~0.8 μm was estimated. Considering the different degree of morphological homogeneity of the layers (Fig. 6), this is a similar trend which was observed for precipitates which formed under potentiostatic control. It seems that in mixed electrolytes with Ca- and Sr-ions, also under galvanostatic pulse control an increasing Sr-ion concentration results in a higher Sr-content in the deposit but retards the layer growth rate. This may be attributed to a steric hindrance of the growing HAp lattice during the precipitation reaction under involvement of both ionic species.

3.4. Release studies with galvanostatically pulse-deposited Sr-substituted Hap layers

Throughout the study it was revealed that galvanostatically pulse-deposited Sr10 layers were the most stable and best adhesive on Ti-45Nb substrates. Therefore, they were employed for further principal release studies by means of ICP-OES. In a first step, the mean elemental concentrations of Ca, P and Sr of layers which were deposited onto a Ti-45Nb substrate were determined and are summarized in Table 2. The resulting Sr/(Ca + Sr) ratio is significantly lower than that for the Sr10 electrolyte which confirms the conclusion from EDX analysis that much less Sr-ions than offered in the source electrolyte are incorporated in the electrodeposited coating. Moreover, the present ratio is lower than that determined by means of EDX, but is here representative for the bulk coating. Considering the GD-OES results this is another hint for an inhomogeneous cross sectional distribution of Sr in the layer. The calculated (Ca + Sr)/P ratio is close to the ratio in the electrolyte and to the theoretical one and confirms in accordance with EDX and XRD analyses the main presence of a stoichiometric hydroxyapatite phase.

In a next step Sr10 samples were subjected to release tests, i.e. they were immersed in TBS (TRIS-buffered saline) at 310 K for up to 1 week according to DIN EN ISO 10993-15 conditions. The determined mean

Table 2

ICP-OES analysis: contents of Ca, P, Sr in layers obtained by galvanostatic pulse deposition in Sr10 electrolyte and calculated concentration ratios in comparison to those of the electrolyte.

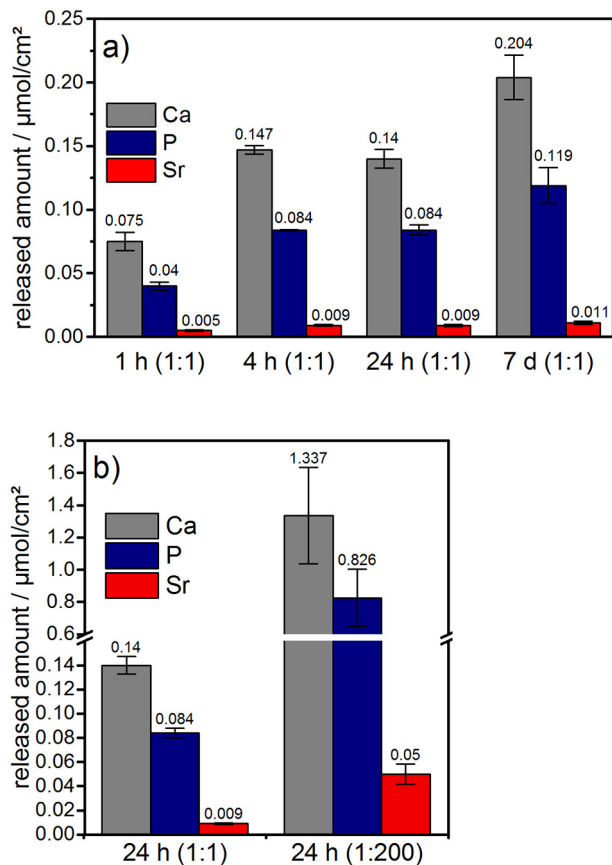| Ca [μmol/cm^2]	P [μmol/cm^2]	Sr [μmol/cm^2]	Sr/(Ca + Sr) ratio	(Ca + Sr)/P ratio
5.14 ± 0.20	3.23 ± 0.14	0.17 ± 0.011	0.03 ± 0.001	1.65 ± 0.012
Electrolyte Sr10 (nominal)			0.1	1.67

Fig. 10. ICP-OES analysis: release of Ca, Sr, and P from a galvanostatically pulse-deposited Sr10 layer upon immersion for 7 days in TBS (pH 7.6) at 310 K with surface:volume ratio of 1:1 according to DIN EN ISO 10993-15 (a) and comparison of release rates after 24 h at ratios of 1:1 and 1:200 (b).

Fig. 11. Proliferation of osteogenically stimulated (OS +) hBMSC over 21 days in contact with the extracts from mechanically ground Ti-45Nb substrates, Ti-45Nb substrates electrochemically coated with Sr-HAp (Sr10) and without material (control) as determined by intracellular LDH activity (a); osteogenic differentiation as determined by specific ALP activity measurement (b); significant differences ($p \le .05$) of selected samples are indicated (Student t-test $n = 3$).

concentrations of released Ca, P and Sr species are shown in Fig. 10a. After an initial burst in the first hour of immersion the release of Ca, P and Sr levels out up to 24 h and increases afterwards only slightly. The release kinetics from the deposit observed in the present study is similar to that reported by Drevet et al. [32] for a Sr-substituted Ca-phosphate coating which was pulse-electrodeposited onto Ti-6Al-4V substrates under similar conditions. After immersion in DMEM they determined 0.6–1 ppm Sr-species in solution. In the present study, after immersion of Sr10 layers in TBS for 1 week a released Sr-ion concentration of ~0.01 μmol/cm^2 corresponding to ~0.6 ppm (referred to a geometrical coating area of 1 cm^2) was determined. This concentration is quite low and indicates that after 1 week immersion the layer still possesses ~94% of its Sr-content. According to DIN EN ISO 10993-15 [36], the applied ratio of the immersed sample surface to the volume of immersion solution was 1:1 under static (natural convection) conditions. A critical problem can be that due to the small solution volume already after 24 h a saturation level in the release process is reached. Released species can re-precipitate as Ca-phosphates on the sample surface. An equilibrium between release and re-precipitation is reached which can explain the only slight further increase of released Ca, P and Sr species after 24 h. These conditions are not perfectly relevant for application
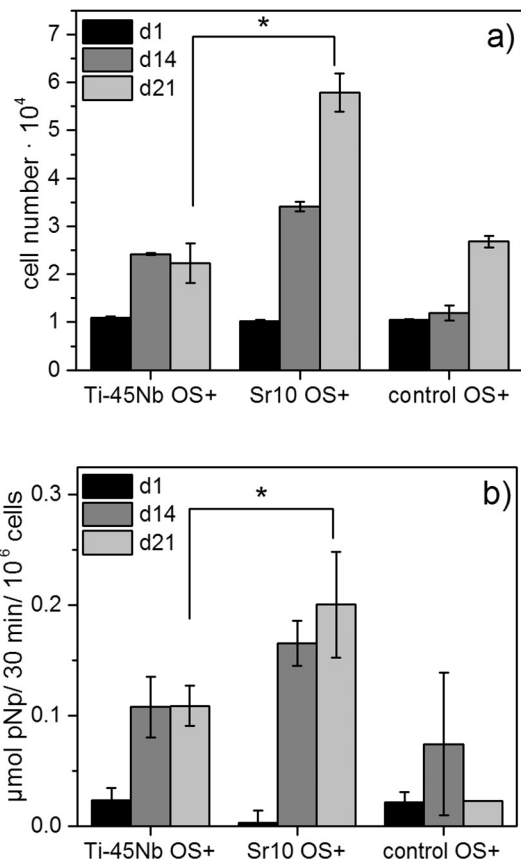
conditions in the human body, where body fluids are under flow and therefore, species concentration change with time. In order to simulate a state that is closer to those dynamic conditions and to avoid saturation effects, Sr10 samples were immersed in a much larger TBS volume corresponding to a surface:volume ratio of 1:200. Results shown in Fig. 10b demonstrate that after 24 h of immersion release rates of Ca, P and Sr are significantly higher, i.e. 5–6 times than at a 1:1 ratio. The amount of released Sr is now about 30–35% of that what was analyzed in electrodeposited Sr10 layers. This indicates that there is a strong need to identify appropriate test conditions for reliable release analysis for those newly developed Sr-substituted HAp coatings.

3.5. Effect of Sr-substituted hap layers on the in vitro behavior of hBMSC

Primary goal of the electrochemical deposition of Sr-modified HAp layers on metallic implant materials is the manipulation of the equilibrium of osteoblast and osteoclast activities in systemically diseased bones in order to support bone tissue formation. The release of Sr-
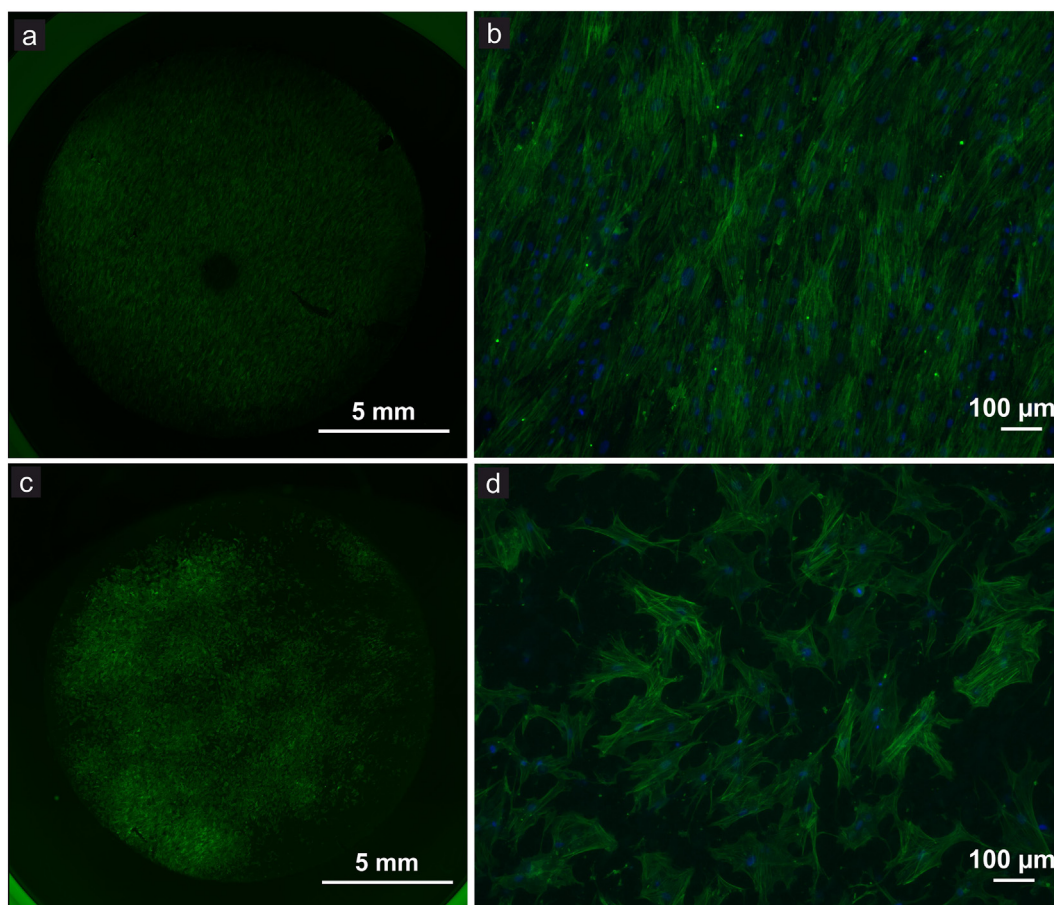
Fig. 12. Fluorescence staining micrographs, demonstrating osteogenically stimulated hBMSC spreading and cytoskeletal organization after 14 days of culture on mechanically ground Ti-45Nb (a, b) and electrochemically coated Ti-45Nb (Sr10) (c, d). Confocal microscopic images with dual staining of cell nuclei (DAPI, blue) and actin filaments (Phalloidin-Alexa 488®, green). (For interpretation of the references to colour in this figure legend, the reader is referred to the web version of this article.)

species from Sr10 layers has been described and discussed already in Section 3.4. For the following in vitro tests those samples were subjected to gamma sterilization. During this and also throughout the whole complex cell testing procedure (Section 2.4) the coatings remained visually mechanical stable and did not change their appearance.

To study the effect of the released ions on osteogenic cells, osteogenically induced (OS+) hBMSC were exposed to medium extracts of coated samples. The study focused on the viability and proliferation as well as osteogenic differentiation of the cells over a period of 3 weeks.

The number of viable cells was determined by the activity of the intracellular enzyme LDH. In Fig. 11a results of the indirect cell culture for uncoated (as ground and passivated) and Sr10-coated Ti-45Nb substrates are shown; as control hBMSC were cultured in medium which was not in contact with material. An increasing number of cells was determined for all 3 groups up to day 14, indicating cell proliferation. In case of uncoated Ti-45Nb samples the cell number does not further increase after 14 days of culture. For the electrochemically coated samples (Sr10) a significant increase in cell number was determined up to day 21 compared to the uncoated samples. The Sr-HAp coated Sr10 samples show herewith the highest cell number and thus, proliferation of all considered conditions. Osteogenic differentiation was assessed according to the ALP activity (Fig. 11b). For all considered groups the ALP activity increases up to day 14. In case of the Sr10 samples it further increases significantly up to day 21 compared to the Ti-45Nb samples and shows herewith also the highest ALP activity for all considered conditions. Taken together, it was demonstrated that the proliferation and osteogenic differentiation of osteogenically stimulated

hBMSC was not negatively affected by the extracts of mechanically ground and electrochemically coated Ti-45Nb samples. For the samples coated with Sr-HAp the data indicate a positive impact of the released ions on proliferation and osteogenic differentiation of hBMSC. Based on the data of ion quantification in the extracts of Sr10 samples (Fig. 10a), we assume that this effect can be predominantly attributed to the Sr^{2+} ions in the extracts whose concentration is, although low in this experimental setup, still within the biologically effective range [21,22]. The released Ca^{2+} and phosphate ions resulted only in a marginal increase of the Ca^{2+} and phosphate ions usually present in the cell culture medium (1.8 mM Ca^{2+} and 1 mM PO_4^{3-} in alpha-MEM). Reports in the literature revealed a stimulating effect of elevated Ca^{2+} and PO_4^{3-} concentrations on proliferation and osteogenic differentiation of MSC, but at significantly higher concentrations [48,49] making a significant effect of Ca^{2+} and phosphate released from the Sr-HAp coating in the present study unlikely.

From the direct cell culture of the hBMSC on the substrates the morphology and distribution of the cells was determined by means of fluorescence microscopy. In Fig. 12 the cell morphology of osteogenically stimulated hBMSC on Ti-45Nb (mechanically ground) and on Ti-45Nb electrochemically coated with Sr-HAp are shown after 14 days of culture. The cell distribution on Sr10 samples compared to the Ti-45Nb samples is quite inhomogeneous, as it is obvious from the overview in Fig. 12c. The partially high cell densities might originate from a locally difference in thickness of the deposit. In the higher magnification of the fluorescence images (Figs. 12b,d) widely spread cells are visible for both considered states indicating support of cell adhesion, which is a good hint on the excellent compatibility of the osteogenically

stimulated hBMSC with the material surface. Based on literature data, the biomimetic HAp coating obtained by electrochemical deposition leads us to expect an enhanced osseointegration (bone-to-implant contact) in comparison to uncoated surfaces [50,51] which might be especially beneficial in osteoporotic conditions [52]. Moreover, a stronger promotion of early bone formation was demonstrated for HAp coatings deposited by soaking in PBS on pre-oxidized Ti implants if it was doped with Sr-ions in a healthy rat tibia defect model [34]. In an osteoporotic rat femur defect model, new bone formation and osseointegration was enhanced by Sr-substituted HAp coatings of Ti implants in a concentration-dependent manner [53].

4. Summary and conclusions

Aim of the present work was to assess suitable approaches for electrodeposition of Sr-substituted hydroxyapatite coatings on surfaces of the low modulus beta-Ti-45Nb alloy and to analyze the Ca, Sr and P release from those coatings as well as the in vitro response of hBMSC.

Potentiodynamic polarization studies in 1.67 mmol/L $Ca(NO_3)_2$ and 1.0 mmol/L $NH_4H_2PO_4$ electrolyte at 333 K revealed the electrochemical steps for the generation of PO_4^{3-} and OH^- which are reactants for a chemical precipitation of $Ca_{10}(PO_4)_6(OH)_2$ hydroxyapatite (HAp) [38–40]. Partial substitution of Ca^{2+}-ions by 10% or 50% Sr^{2+} ions inhibits the overall charge transfer on the Ti-45Nb cathode and leads to Sr-substituted compounds (Srx-HAp).

From *potentiostatic deposition studies* at moderate cathodic potentials of −1.2 V to −1.5 V vs. Ag/AgCl the initial formation of phases of low crystallinity is concluded which gradually block the Ti-45Nb surface and can act as seed layers for the chemical precipitation of (Sr-substituted) hydroxyapatite. In electrolytes with no or 10% Sr-nitrate, coatings with plate-like morphology are formed while higher Sr-nitrate fractions up to 100% lead to fine-needle-like structures.

Upon *galvanostatic pulse-deposition* electrochemical reaction rates are enhanced with impact on the subsequent chemical precipitations. All deposits comprised only a hydroxyapatite phase with high crystallinity and fine needle-like shape of 200–300 nm size. For layers formed in electrolytes with 10% and 50% Sr-nitrate substitution, the Sr-distribution is laterally homogeneous but non-homogeneous along their cross-section. An increasing Sr-ion concentration resulted in a higher Sr-content in the deposit but retarded the layer growth which may be due to a steric hindrance of the growing Srx-HAp lattice. The Srx-HAp layer-type from the electrolyte with 10% Sr-substitution had a typical Sr/(Ca + Sr) ratio of 0.03 and the highest thickness of about 3 μm and was most stable and adhesive to the substrate. For that release analysis was done in TBS at 310 K. At a surface:volume ratio of 1:200, after 24 h the amount of released Sr-ions was about 30–35% of that determined in the coating. In vitro studies with hBMSC revealed the excellent cytocompatibility of the Srx-HAp coating indicated by cell adhesion and proliferation in direct contact. The Sr^{2+}-ions released from the coated samples stimulated proliferation and differentiation of osteogenically induced hBMSC.

Declaration of competing interest.

The authors declare that they have no known competing financial interests or personal relationships that could have appeared to influence the work reported in this paper.

References

[1] M. Niinomi, Y. Liu, M. Nakai, H. Liu, H. Li, Biomedical titanium alloys with Young's moduli close to that of cortical bone, Regen. Biomater. 3 (2016) 173–185, https://doi.org/10.1093/rb/rbw016.

[2] D. Arcos, A.R. Boccaccini, M. Bohner, A. Diez-Perez, M. Epple, E. Gomez-Barrena, A. Herrera, J.A. Planell, L. Rodriguez-Manas, M. Vallet-Regi, The relevance of biomaterials to the prevention and treatment of osteoporosis, Acta Biomater. 10 (2014) 1793–1805, https://doi.org/10.1016/j.actbio.2014.01.004.

[3] H. Matsumoto, S. Watanabe, S. Hanada, Beta TiNbSn alloys with low Young's Modulus and high strength, Mater. Trans. 46 (2005) 1070–1078, https://doi.org/10.2320/matertrans.46.1070.

[4] M. Calin, A. Helth, J.J. Gutierrez-Moreno, M. Bönisch, V. Brackmann, L. Giebeler, T. Gemming, C.E. Lekka, A. Gebert, R. Schnettler, J. Eckert, Elastic softening β-type Ti-40Nb alloys by indium (In) additions, J. Mech. Behav. Biomed. 39 (2014) 162–174, https://doi.org/10.1016/j.jmbbm.2014.07.010.

[5] A. Helth, S. Pilz, T. Kirsten, L. Giebeler, J. Freudenberger, M. Calin, J. Eckert, A. Gebert, Effect of thermomechanical processing on the mechanical biofunctionality of a low modulus Ti-40Nb alloy, J. Mech. Behav. Biomed. Mater. 65 (2017) 137–150, https://doi.org/10.1016/j.jmbbm.2016.08.017.

[6] S. Pilz, D. Geissler, M. Calin, J. Eckert, M. Zimmermann, J. Freudenberger, A. Gebert, Thermomechanical processing of in-containing β-type Ti-Nb alloys, J. Mech. Behav. Biomed. Mater. 79 (2017) 283–291, https://doi.org/10.1016/j.jmbbm.2017.12.028.

[7] A. Helth, P.F. Gostin, S. Oswald, H. Wendrock, U. Wolff, U. Hempel, S. Arnold, M. Calin, J. Eckert, A. Gebert, Chemical nanoroughening of Ti-40Nb surfaces and its effect on human mesenchymal stromal cell response, J. Biomed. Mater. Res. B 102 (2014) 31–41, https://doi.org/10.1002/jbm.b.32976.

[8] A. Gebert, S. Oswald, A. Helth, A. Voss, P.F. Gostin, M. Rohnke, J. Janek, M. Calin, J. Eckert, Effect of indium (In) on corrosion and passivity of a beta-type Ti-Nb alloy in Ringers's solution, Appl. Surf. Sci. 335 (2015) 213–222, https://doi.org/10.1016/j.apsusc.2015.02.058.

[9] S. Pilz, A. Gebert, A. Voss, S. Oswald, M. Goettlicher, U. Hempel, J. Eckert, M. Rohnke, J. Janek, M. Calin, Metal release and cell biological compatibility of beta-type Ti-40Nb containing indium, J. Biomed. Mater. Res. Part B 106B (2018) 1686–1697, https://doi.org/10.1002/jbm.b.33976.

[10] P. Tengvall, I. Lundström, L. Sjöqvist, H. Elwing, L.M. Bjursten, Titanium-hydrogen peroxide interaction: model studies of the influence of the inflammatory response on titanium implants, Biomaterials 10 (1989) 166–175, https://doi.org/10.1016/0142-9612(89)90019-7.

[11] L. Baldwin, J.A. Hunt, Host inflammatory response to NiCr, CoCr, and Ti in soft a soft tissue implantation model, J. Biomed. Mater. Res. Part A 79A (2006) 574–581, https://doi.org/10.1002/jbm.a.

[12] X. Liu, P. Chu, C. Ding, Surface modification of titanium, titanium alloys, and related materials for biomedical applications, Mater. Sci. Eng. R Reports. 47 (2004) 49–121, https://doi.org/10.1016/j.mser.2004.11.001.

[13] N. Eliaz, N. Metoki, Calcium phosphate bioceramics: a review of their history, structure, properties, coating technologies and biomedical applications, Materials (Basel) 10 (2017) 334–340, https://doi.org/10.3390/ma10040334.

[14] V. Uskokovic, The role of hydroxyl channel in defining selected physicochemical peculiarities exhibited by hydroxyapaptite, RSC Adv. 5 (2015) 36614–36633, https://doi.org/10.1039/c4ra17180b.

[15] S. Yin, D.E. Ellis, First-principles investigations of Ti-substituted hydroxyapatite electronic structure, Phys. Chem. Chem. Phys. 12 (2010) 156–163, https://doi.org/10.1039/B915171K.

[16] E. Boanini, M. Gazzano, a. Bigi, Ionic substitutions in calcium phosphates synthesized at low temperature, Acta Biomater. 6 (2010) 1882–1894, https://doi.org/10.1016/j.actbio.2009.12.041.

[17] J. Terra, E.R. Dourado, J.-G. Eon, D.E. Ellis, G. Gonzalez, A.M. Rossi, The structure of strontium-doped hydroxyapatite: an experimental and theoretical study, Phys. Chem. Chem. Phys. 11 (2009) 568–577, https://doi.org/10.1039/B802841A.

[18] H.B. Pan, Z.Y. Li, W.M. Lam, J.C. Wong, B.W. Darwell, K.D.K. Luk, W.W. Lu, Solubility of strontium-substituted apatite by solid titration, Acta Biomater. 5 (2009) 1678–1685, https://doi.org/10.1016/j.actbio.2008.11.032.

[19] E. Bonnelye, A. Chabadel, F. Saltel, P. Jurdic, Dual effect of strontium ranelate: stimulation of osteoblast differentiation and inhibition of osteoclast formation and resorption in vitro, Bone 42 (2008) 129–138, https://doi.org/10.1016/j.bone.2007.08.043.

[20] J. Braux, F. Velard, C. Guillaume, S. Bouthors, E. Jallot, J.-M. Nedelec, D. Laurent-Maquin, P. Laquerrière, A new insight into the dissociating effect of strontium on bone resorption and formation, Acta Biomater. 7 (2011) 2593–2603, https://doi.org/10.1016/j.actbio.2011.02.013.

[21] J.T.B. Ratnayake, M. Mucalo, G.J. Dias, Substituted hydroxyapatites for bone regeneration: a review of current trends, J. Biomed. Mater. Res. - Part B Appl. Biomater. 105 (2017) 1285–1299, https://doi.org/10.1002/jbm.b.33651.

[22] M. Schumacher, A.S. Wagner, J. Kokesch-Himmelreich, A. Bernhardt, M. Rohnke, S. Wenisch, M. Gelinsky, Strontium substitution in apatitic CaP cements effectively attenuates osteoclastic resorption but does not inhibit osteoclastogenesis, Acta Biomater. 37 (2016) 184–194, https://doi.org/10.1016/j.actbio.2016.04.016.

[23] J. Isaac, J. Nohra, J. Lao, E. Jallot, J.M. Nedelec, A. Berdal, J.M. Sautier, Effects of strontium doped bioactive glass on the differentiation of cultured osteogenic cells, Eur. Cell. Mater. 21 (2011) 130–143, https://doi.org/10.22203/eCM.v021a11.

[24] T.J. Levingstone, M. Ardhaoui, K. Benyounis, L. Looney, J.T. Stokes, Plasma sprayed hydroxyapatite coatings: understanding process relationsships using design of experiment analysis, Surf. Coat. Tech. 283 (2015) 29–36, https://doi.org/10.1016/j.

surfcoat.2015.10.044.

[25] Y.P. Lu, M.S. Li, S.T. Li, Z.G. Wang, R.F. Zhu, Plasma-sprayed hydro-xyapatite + titania composite bond coat for hydroxyapatite coating on titanium substrate, Biomaterials 25 (2004) 4393–4403, https://doi.org/10.1016/j.biomaterials.2003.10.092.

[26] M. Sadat-Shojai, M.T. Khorasani, E. Dinpanah-Khoshdargi, A. Jamshidi, Synthesis methods for nanosized hydroxyapatite with diverse structures, Acta Biomater. 9 (2013) 7591–7621, https://doi.org/10.1016/j.actbio.2013.04.012.

[27] W. Xia, C. Lindahl, J. Lausmaa, P. Borchardt, A. Ballo, P. Thomson, H. Engqvist, Biomineralized strontium-substituted apatite/titanium dioxide coating on titanium surfaces, Acta Biomater. 6 (2010) 1591–1600, https://doi.org/10.1016/j.actbio.2009.10.030.

[28] K. Zhuravleva, A. Chivu, A. Teresiak, S. Scudino, M. Calin, L. Schultz, et al., Porous low modulus Ti40Nb compacts with electrodeposited hydroxyapatite coating for biomedical applications, Mater. Sci. Eng. C Mater. Biol. Appl. 33 (2013) 2280–2287, https://doi.org/10.1016/j.msec.2013.01.049.

[29] R. Drevet, H. Benhayoune, L. Wortham, S. Potiron, J. Douglade, D. Laurent-Maquin, Effects of pulsed current and H_2O_2 amount on the composition of electrodeposited calcium phosphate coatings, Mater. Characterization 61 (2010) 786–795, https://doi.org/10.1016/j.matchar.2010.04.016.

[30] D. Gopi, J. Indira, K. Kavitha, A comparative study on the direct and pulsed current electrodeposition of hydroxyapatite coatings on surgical grade stainless steel, Surf. Coatings Technol. 206 (2012) 2859–2869, https://doi.org/10.1016/j.surfcoat.2011.12.011.

[31] R. Schmidt, V. Hoffmann, A. Helth, P.F. Gostin, M. Calin, J. Eckert, A. Gebert, Electrochemical deposition of hydroxyapatite on beta-Ti-40Nb, Surf. Coatings Technol. 294 (2016) 186–193, https://doi.org/10.1016/j.surfcoat.2016.03.063.

[32] R. Drevet, H. Benhayoune, Pulsed electrodeposition for the synthesis of strontium-substituted calcium phosphate coatings with improved dissolution properties, Mater. Sci. Eng. C Mater. Biol. Appl. 33 (2013) 4260–4265, https://doi.org/10.1016/j.msec.2013.06.019.

[33] C. Wolf-Brandstetter, S. Oswald, S. Bierbaum, H.-P. Wiesmann, D. Scharnweber, Influence of pulse ratio on codeposition of copper species with calcium phosphate coatings on titanium by means of electrochemically assisted deposition, J Biomed Mater Res B Appl Biomater 102 (2014) 160–172, https://doi.org/10.1002/jbm.b.32992.

[34] A.M. Ballo, W. Xia, A. Palmquist, C. Lindahl, L. Emanuelsson, J. Lausmaa, H. Engqvist, P. Thomsen, Bone tissue reactions to biomimetic ion-substituted apatite surfaces on titanium implants, J. R. Soc. Interface 9 (2012) 1615–1624, https://doi.org/10.1098/rsif.2011.0808.

[35] J. Yan, J. Sun, P.K. Chu, Y. Han, Y. Zhang, Bone integration capability of a series of strontium-containing hydroxyapatite coatings formed by micro-arc oxidation, J. Biomed. Mater. Res. Part A 101A (2013) 2465–2480, https://doi.org/10.1002/jbm.a.34548.

[36] DIN EN ISO 10993-15, Biological Evaluation of Medical Devices - Part 15: Identification and Quantification of Degradation Products from Metals and Alloys, (2009) 10.

[37] M. Schumacher, A. Lode, A. Helth, M. Gelinsky, A novel strontium(II)-modified calcium phosphate bone cement stimulates hMSC proliferation and osteogenic differentiation in vitro, Acta Biomater. 9 (2013) 9547–9557, https://doi.org/10.1016/j.actbio.2013.07.027.

[38] M.C. Kuo, S.K. Yen, The process of electrochemical deposited hydroxyapatite coatings on biomedical titanium at room temperature, Mater. Sci. Eng. C. 20 (2002) 153–160, https://doi.org/10.1016/S0928-4931(02)00026-7.

[39] S. Joseph, P. Vishnu Kamath, Electrodeposition of oriented $SrCO_3$ coatings on stainless steel substrates, J. Electrochem. Soc. 153 (2006) D99–D102, https://doi.org/10.1149/1.2188129.

[40] M. Pourbaix, Atlas of Electrochemical Equilibria in Aqueous Solutions, Pergamon Press, Oxford, 1966.

[41] S.K. Yen, C.M. Lin, Cathodic reactions of electrolytic hydroxyapatite coating on pure titanium, Mater. Chem. Phys. 77 (2003) 70–76, https://doi.org/10.1016/S0254-0584(01)00562-4.

[42] E.D. Eanes, A.S. Posner, Intermediate phases in the basic solution preparation of alkaline earth phosphates, Calcif. Tissue Res. 2 (1968) 38–48, https://doi.org/10.1007/BF02279192.

[43] R.L. Collin, Precipitate formation in the strontium-phosphate system, Science 151 (1966) 1386–1388, https://doi.org/10.1126/science.151.3716.1386.

[44] P. Atkins, J. dePaula, Physical Chemistry, 8thed., Oxford Univ. Press, Oxford, 2006.

[45] N. Eliaz, T.M. Sridhar, Electrocrystallization of hydroxyapatite and its dependence on solution conditions, Cryst. Growth Des. 8 (2008) 3965–3977, https://doi.org/10.1021/cg800016h.

[46] T.V. Vijayaraghavan, A. Bensalem, Electrodeposition of apatite coating on pure titanium and titanium alloys, J. Mater. Sci. Lett. 13 (1994) 1782–1785, https://doi.org/10.1007/BF00776358.

[47] M. Manso, C. Jiménez, C. Morant, P. Herrero, J.M. Martínez-Duart, Electrodeposition of hydroxyapatite coatings in basic conditions, Biomaterials 21 (2000) 1755–1761, https://doi.org/10.1016/S0142-9612(00)00061-2.

[48] A. González-Vázquez, J.A. Planell, E. Engel, Extracellular calcium and CaSR drive osteoinduction in mesenchymal stromal cells, Acta Biomater. 10 (2014) 2824–2833, https://doi.org/10.1016/j.actbio.2014.02.004.

[49] C.B.S.S. Danoux, D.C. Bassett, Z. Othman, A.I. Rodrigues, R.L. Reis, J.E. Barralet, C.A. van Blitterswijk, P. Habibovic, Elucidating the individual effects of calcium and phosphate ions on hMSCs by using composite materials, Acta Biomater. 17 (2015) 1–15, https://doi.org/10.1016/j.actbio.2015.02.003.

[50] J.E. Biemond, T.S. Eufrasio, G. Hannink, N. Verdonschot, P. Burma, Assessment of bone ingrowth potential of biomimetic hydroxyapatite and brushite coated porous e-beam structures, J. Mater. Sci. Mater. Med. 22 (2011) 917–925, https://doi.org/10.1007/s10856-011-4256-0.

[51] D. Mathew, G. Bhardwaj, Q. Wang, L. Sun, B. Ercan, M. Geetha, T.J. Webster, Decreased staphylococcus aureus and increased osteoblast density on nanostructured electrophoretic-deposited hydroxyapatite on titanium without the use of pharmaceuticals, Int. J. Nanomedicine 9 (2014) 1775–1781, https://doi.org/10.2147/IJN.S55733.

[52] H.S. Alghamdi, V.M.J.I. Cuijpers, J.G.C. Wolke, J.J.J.P. van den Beucken, J.A. Jansen, Calcium-phosphate-coated oral implants promote osseointegration in osteoporosis, J. Dent. Res. 92 (2011) 982–988, https://doi.org/10.1177/0022034513505769.

[53] Z.S. Tao, B.L. Bai, X.W. He, W. Liu, H. Li, Q. Zhou, T. Sun, Z.L. Huang, K.K. Tu, Y.X. Lv, A comparative study of strontium-substituted hydroxyapatite coating on implant's osseointegration for osteopenic rats, Med. Biolog. Eng. Comput. 54 (2016) 1959–1968, https://doi.org/10.1007/s11517-016-1494-9.